Oxygen permeability of Fe-Ni-Cr alloys at 1100 and 1150 °C under carbon-free and carbon-containing gases

Domingo Jullian, Aurélien Prillieux, Jianqiang Zhang, David J. Young

DOI: 10.1002/maco.201508803

Oxygen permeability of Fe-Ni-Cr alloys at 1100 and 1150 °C under carbon-free and carbon-containing gases

D. Jullian, A. Prillieux, J. Zhang* and D.J. Young

Wagner's model of internal oxidation allows the prediction of an alloy's critical concentration of oxide forming metal required to achieve a protective oxide scale at high temperatures. The model depends on oxygen permeability in the alloy, but this parameter has not been evaluated for the Fe-Ni system, and the influence of carbon-bearing gases is unknown. Oxygen permeability measurement by internal oxidation of Fe-Ni-Cr alloys, reacted at 1100 and 1150 °C is described. Exposures in Rhines packs and flowing CO-CO_2 gas mixtures serve to assess the influence of carbon on oxygen permeability at the Fe-FeO equilibrium oxygen potential. Oxygen permeability in Fe-Ni increases with iron content in a non-ideal manner in both gas environments. Higher permeability is found in carbon bearing gases for iron-rich alloys, and the size of this effect increases with temperature.

1 Introduction

Oxidation resistance of high temperature alloys relies on the formation of a slow growing, thermodynamically stable oxide scale, which acts as a barrier for inwards oxygen diffusion. Elements such as chromium, aluminium or silicon are typically employed for this purpose. In order to achieve the formation of a protective oxide scale, the alloy must contain a minimum concentration of the oxide forming element [1]. This is for two primary purposes: 1) to achieve the transition from internal to external oxidation; and 2) to provide a diffusive flux of protective element toward the scale to enable its sustained growth and reformation in case of spalling.

The critical concentration of oxide-forming element to achieve the transition from internal to external oxidation was first calculated by *Wagner* [1], on the assumption that the formation of internal oxides blocks the inward flux of oxygen. This mechanism allows chromium to diffuse from the matrix, promoting sideways growth of the internal oxides until eventually a continuous scale is formed. The critical concentration $N_B^{(0)}(crit)$ can be predicted from

$$N_B^{(0)}(crit) = \left(\frac{f_V^* V_{Alloy} N_O^{(s)} D_O}{2\nu V_{Ox} \tilde{D}_B} \right)^{1/2} \quad (1)$$

D. Jullian, A. Prillieux, J. Zhang, D.J. Young
School of Materials Science and Engineering, UNSW Australia, Sydney, NSW 2052 (Australia)
E-mail: j.q.zhang@unsw.edu.au

A. Prillieux
CIRIMAT, Université de Toulouse, CNRS, INPT, UPS, ENSIACET 4 allée Emile Monso, BP-44362, 31030, Toulouse Cedex 4 (France)

where B refers to the protective oxide forming element, f_V^* is the critical oxide volume fraction needed for the transition from internal to external oxidation, which is usually taken to be 0.3, following the study of *Rapp* [2] on silver-indium alloys. Recent studies by *Leblond* [3] and *Zhao* et al. [4] showed that this factor is not constant and depends on factors such as the molar volumes of the species and the internal oxide morphology. The quantites V_{Alloy} and V_{Ox} refer to the molar volume of the alloy and the internal oxide, respectively, ν is the stoichiometric coefficient for oxide BO_ν, $\tilde{D}_B$ the interdiffusion coefficient of the oxide forming element in the alloy, $N_O^{(s)}$ the concentration of dissolved oxygen on the surface of the metal, and D_O the diffusion coefficient of oxygen in the alloy. The product of the last two quantities is referred to as oxygen permeability.

Another important factor in the study of protective oxide scale formation is the presence of secondary oxidants, for example, carbon dioxide and/or water vapor in the combustion gas. It has been reported that both carbon dioxide and water vapor accelerate alloy oxidation at high temperature [5–7]. Unfortunately, the effect of these secondary oxidants on oxygen permeability is unknown.

Oxygen permeability has been determined for pure iron [8] and nickel [9,10], however, no information is available for the iron-nickel system.

2 Theoretical basis for determination of oxygen permeability

When an internal oxidation process is controlled by diffusion, and the rate is not determined by a surface reaction, then the depth of penetration of the internal oxide front into the alloy, X_i,

increases according to parabolic kinetics:

$$X_i^2 = 2k_p^{(i)}t \tag{2}$$

where $k_p^{(i)}$ is the parabolic rate constant of internal oxidation. A particular case of internal oxidation occurs when oxygen permeability is much higher than the product of the bulk alloy oxide forming metal content, $N_B^{(0)}$, and its interdiffusion coefficient, as stated by:

$$N_O^{(s)}D_O \gg N_B^{(0)}\tilde{D}_B \tag{3}$$

In cases when Equation (3) is satisfied, *Wagner* [1] showed that the parabolic rate constant is proportional to the oxygen permeability:

$$k_p^{(i)} = \frac{N_O^{(s)}D_O}{\nu N_B^{(0)}} \tag{4}$$

Using this fomula, oxygen permeability can be determined indirectly by conducting internal oxidation experiments and measuring $k_p^{(i)}$ for alloys with low $N_B^{(0)}$.

Chromium is particularly well-suited as an alloy solute in experiments of this sort, since its oxides tend to precipitate as spheroidally shaped, discrete particles [11]. This is in contrast with aluminium alloys, which tend to form needle-shaped precipitates oriented perpendicularly to the alloy surface, thereby providing pathways for short circuit diffusion and giving rise to a higher apparent permeability [12].

The aim of this work was to determine oxygen permeability of the iron-nickel system at high temperatures and assess the effect of carbon bearing gases on this parameter.

3 Experimental

Internal oxidation of Fe-Cr and Fe-Ni-Cr was carried out in model alloys, at 1100 and 1150 °C.

3.1 Materials

The alloys were arc-melted in Ar-5%H_2 gas from high purity iron (99.98%), nickel (99.995%), and chromium (99.99%) using non-consumable electrodes. Alloy compositions were formulated with increasing iron-nickel ratios (Table 1). Three chromium levels of 2, 4, and 7.5% (all in at%) were studied, excepting for the highest nickel content alloy, where 1% chromium was employed, as the 7.5% chromium alloy forms an external oxide scale. All alloys are austenitic at the reaction temperatures.

All alloys were annealed under flowing hydrogen at 1100 °C for 72 h to ensure homogenization and reduction of any surface oxides. After annealing, the alloys were cut into slices of thickness 1.3 mm and then ground to a 4000 grit finish using SiC paper. The slices were ultrasonically cleaned in ethanol and dried before reaction.

Table 1. Alloy composition

Alloy	Fe at%	Ni at %	Cr at%	$\frac{N_{Fe}}{(N_{Fe}+N_{Ni})}$
AA	98	0	2	1
AB	96	0	4	1
AC	92.5	0	7.5	1
BA	78.4	19.6	2	0.8
BB	76.8	19.2	4	0.8
BC	74	18.5	7.5	0.8
CA	58.8	39.2	2	0.6
CB	57.6	38.4	4	0.6
CC	55.5	37	7.5	0.6
DA	39.2	58.8	2	0.4
DB	38.4	57.6	4	0.4
DC	37	55.5	7.5	0.4
EA	19.8	79.2	1	0.2
EB	19.6	78.4	2	0.2
EC	19.2	76.8	4	0.2

3.2 Gas composition

The samples were subsequently oxidized under gas mixtures with an oxygen partial pressure corresponding to the Fe-FeO equilibrium. Gas mixtures with and without carbon were employed, using flowing CO-CO_2 gas mixtures and Rhines packs.

3.2.1 Rhines packs

Experiments under carbon-free gas mixtures were conducted using Rhines packs [13]. The samples were oxidized in vacuum-sealed quartz capsules, which contained a mixture of powdered iron and wüstite. The equilibrium reaction between these two phases controlled the oxygen potential inside the capsule. A powder mixture (Fe:FeO molar ratio of 2:3) of 2 g was placed in each capsule, providing a large excess of oxygen relative to the amount of chromium being oxidized. Alloy samples were physically separated from the powder by a constriction in the cylindrical capsule.

The Fe-FeO mixture was synthesized from pure iron powder reacted for 5 h at 950 °C under Ar-5%H_2 saturated with water vapor at 58 °C. The oxide phase was characterized by X-ray diffraction (XRD) and the fraction of oxide was determined by mass gain. The mixture was then ground with mortar and pestle and sieved to particle sizes of 100–850 μm. Analysis by XRD revealed the phase constitution of Fe-FeO was preserved after the reaction in the Rhines packs, demonstrating a stable oxygen potential.

3.2.2 CO-CO_2 gas mixtures

Alloy samples were exposed in a horizontal tube furnace to a flowing CO-CO_2 gas mixture regulated using mass flow controllers. The gas mixture was set at each temperature so as to obtain the same oxygen partial pressure of the Fe-FeO equilibrium, as shown in Table 2. High purity gases were employed to avoid moisture and its influence on oxygen potential [14]. Accurate control of the oxygen partial pressure

Table 2. Oxygen partial pressure of Fe-FeO equilibrium and carbon activity of CO-CO_2 gas mixtures

T (°C)	pO_2 (atm)	pCO/pCO_2	a_C ($P_{tot} = 1$ atm)
1150	2.43×10^{-13}	2.96	0.003
1100	4.76×10^{-14}	2.81	0.005

was monitored by including a slice of pure iron in each experimental run and verifying that only small FeO particles formed on the surface rather than a continuous FeO scale over the whole metal surface. Calculated carbon activities were low and none of the chromium carbides was thermodynamically stable.

3.3 Reaction times

Samples were reacted for the times shown in Table 3. Because oxygen diffusivity is lower in nickel than in iron [9,15], internal oxidation experiments were separated in two groups: high iron content alloys ($N_{Fe} > 0.5$), and high nickel content alloys ($N_{Ni} > 0.5$).

3.4 Specimen characterisation

After reaction, Rhines packs were quenched in water. For experiments under CO-CO_2 gas, samples were moved to the cold zone of the furnace. Reacted samples were metallographically cross-sectioned, and internal oxide penetration depths measured from optical micrographs using ImageJ image analysis software. In cases where the sample surface was locally oxidized, measurements were performed in the unaffected metal surface.

Sample surfaces were characterized using XRD, and cross-sections were analysed with scanning electron microscopy (SEM) together with energy dispersive X-ray spectroscopy (EDS).

4 Results

4.1 Internal oxidation microstructure

Internal oxidization zones contained discrete oxide precipitates in all cases. No preferential precipitate growth orientation was observed, consistent with previous studies [16]. Typical examples of this structure are shown in Figs. 1 and 2. The oxide particles had a more spherical shape in lower-chromium content alloys and precipitates were coarser at higher chromium levels, as seen in Fig. 1 for alloys with $N_{Fe}/(N_{Fe} + N_{Ni}) = 0.6$, reacted in CO-$CO_2$ at 1150 °C. No preferential penetration developed along grain boundaries as shown in Fig. 1b and c, indicating that grain boundary diffusion is not predominant over bulk diffusion of oxygen.

Oxide morphology was also observed to change with nickel content, with the smallest precipitates obtained in Fe-Cr alloys and size increasing with nickel concentration. The effect is illustrated in Fig. 2 for Fe-Ni-7.5 at% Cr alloys. In the higher nickel alloys, metal nodules were sometimes present on the surface, as shown in Fig. 2d [16,17].

Table 3. Reaction times [h]

	Rhines pack		CO-CO_2	
Alloy	1100 °C	1150 °C	1100 °C	1150 °C
AA to CC	5, 10, 24, 100	4, 8, 16, 48	5, 10, 24, 100	4, 8, 16, 48
DA to EC	48, 100, 150	24, 48, 100, 150	24, 100, 150	24, 48, 100, 150

4.2 Internal oxidation kinetics

Internal oxide penetration kinetics were in good agreement with Equation (2). One example is shown in Fig. 3, for alloys of composition $N_{Fe}/(N_{Fe} + N_{Ni}) = 0.6$ reacted in CO-CO_2 at 1150 °C. Parabolic rate constants obtained by regression are shown in Table 4. It is seen that higher iron content alloys reacted in CO-CO_2 displayed higher penetration rates than in Rhines packs, at both temperatures. The high nickel alloys displayed similar penetration rates at 1150 °C for both environments, while slightly higher penetrations in Rhines packs were observed at 1100 °C.

5 Discussion

Experimental data were used to obtain oxygen permeability values by applying *Wagner's* diffusion theory. The following factors are discussed: chromium enrichment in the internally oxidized zone, dependence of the oxide penetration rates on chromium concentration, the effective stoichiometric coefficient of the internal oxide, and the effect on permeability of the alloy Fe/Ni ratio.

5.1 Chromium enrichment

The formation of chromium oxide during internal oxidation depletes the matrix of chromium and, in consequence, drives its counter-diffusion from the bulk toward the precipitation zone. If the limiting condition of Equation (3) applies, then this counter-diffusion flux is much slower than the inwards flux of oxygen and oxygen transport is the only relevant parameter. However, if chromium counter-diffusion into the internal oxidation zone is not negligible, this leads to chromium enrichment in the internally oxidized zone. As a result, the oxide mole fraction N_{CrO_v}, is higher than the mole fraction of chromium in the bulk. This effect is quantified by the enrichment factor α, defined as

$$\alpha = \frac{N_{CrO_v}}{N_{Cr}^{(0)}} \tag{5}$$

If the conditions of Equation (3) are met, then α is equal to one.

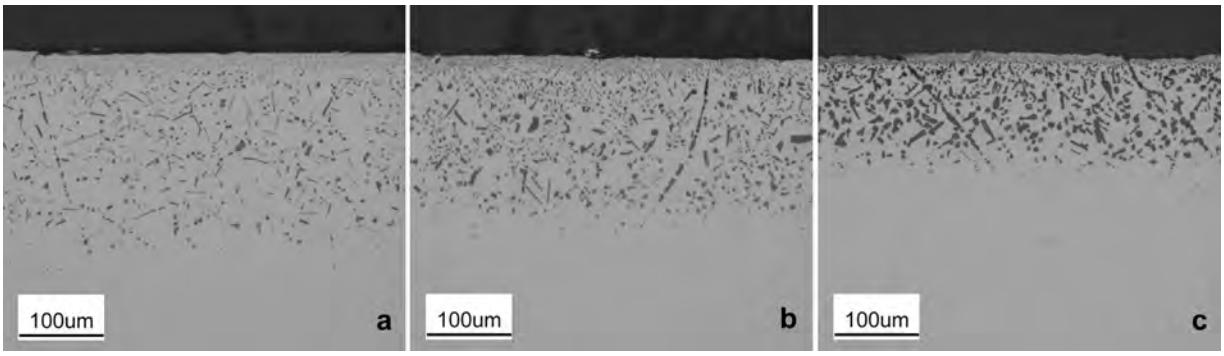

Figure 1. Effect of chromium content of (a) 2 at%, (b) 4 at%, and (c) 7.5 at% on morphology of internal oxide formed in alloy with composition $N_{Fe}/(N_{Fe}+N_{Ni})=0.6$ in $CO\text{-}CO_2$ at 1150 °C

Assuming all chromium in the internal oxidation zone is oxidized, it is possible to obtain the mole fraction of chromium in this zone by measuring the volume fraction of oxide. The enrichment factor is then calculated using

$$\alpha = \frac{1}{N_{Cr}^{(0)}}\left[\frac{f_V V_{Alloy}}{(1-f_V)V_{Ox}+f_V V_{Alloy}}\right] \tag{6}$$

where f_V is the oxide volume fraction.

5.1.1 Measurement of internal oxide volume fraction

The oxide volume fraction was measured by image analysis of the internal oxidation zone of the higher chromium content alloys. High resolution optical micrographs were transformed into binary images, and pixels corresponding to the oxide counted along the direction of the advancing internal oxidation front. Then the total oxide volume fraction was obtained by numerical integration.

Values of the enrichment factor obtained from Equation (6) using measured values of f_V are shown in Table 5. Values are higher than one in all cases, indicating that chromium had diffused into the internal oxidation zone from the bulk.

5.1.2 Calculated enrichment

As proof of chromium enrichment was found in the internally oxidized zone, it follows that Equation (4) is not applicable for all alloys. A less restrictive formulation considers chromium counter-diffusion and incorporates the enrichment factor [1,15]. This is achieved by modifying the mass balance underlying Equation (4), to obtain

$$\alpha k_p^{(i)} = \frac{N_O^{(s)} D_O}{\nu N_{Cr}^{(0)}} \tag{7}$$

The condition [1] for the applicability of Equation (7) is

$$\left(\frac{k_p^{(i)}}{2D_O}\right)^{1/2} \ll 1 \tag{8}$$

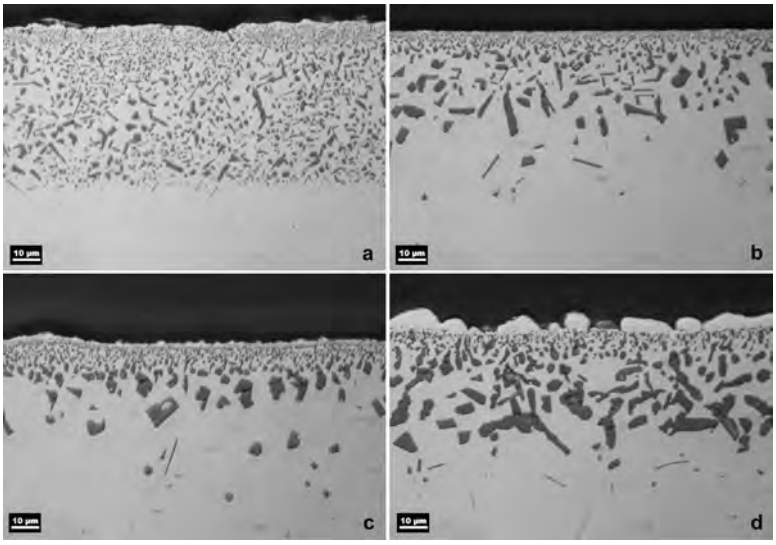

Figure 2. Effect of Ni content, $N_{Ni}/(N_{Ni}+N_{Fe})$ of (a) 0, (b) 0.2, (c) 0.4, and (d) 0.6, on internal oxide morphology of Fe-Ni-7.5%Cr alloys reacted in Rhines packs at 1100 °C for 5 h for (a)–(c) and 48 h for (d)

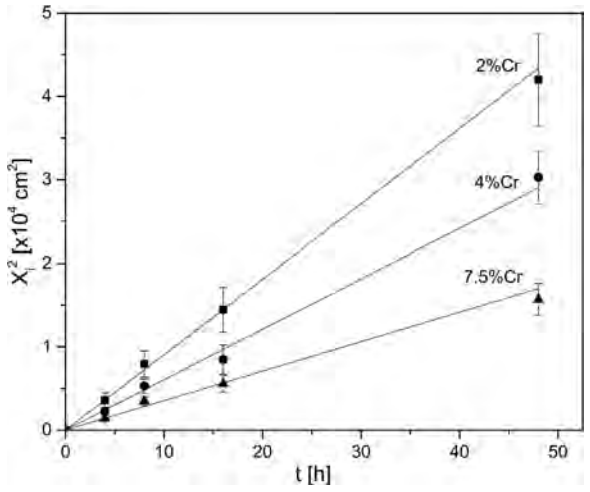

Figure 3. Internal oxidation kinetics for alloys of composition $N_{Fe}/(N_{Fe}+N_{Ni}) = 0.6$ in CO-CO_2 at 1150 °C

This requirement is verified using published values for the diffusion coefficient of oxygen in iron and nickel [8,9]. Thus it is found that $\left(k_p^{(i)}/2D_O\right)^{1/2}$ equals 0.05 for Fe-2Cr and 0.09 for Ni-2Cr [9,10].

Chromium enrichment can also be calculated from *Wagner's* diffusional analysis [1],

$$\alpha = \frac{1}{\pi^{1/2} z \exp(z^2)\mathrm{erfc}(z)} \tag{9}$$

where z is defined as

$$z = \left(\frac{k_p^{(i)}}{2\tilde{D}_{Cr}}\right)^{1/2} \tag{10}$$

Table 4. Parabolic constants of internal oxidation [x 10^{-10} cm^2 s^{-1}]

	Rhines pack		CO-CO_2	
Alloy	1100 °C	1150 °C	1100 °C	1150 °C
AA	14.04	27.39	16.12	39.03
AB	9.32	17.77	8.94	23.71
AC	7.13	13.91	6.95	15.87
BA	9.28	17.35	10.62	22.02
BB	5.92	11.99	6.76	14.06
BC	2.39	6.71	5.20	11.19
CA	4.45	9.62	5.02	12.24
CB	3.86	4.90	3.20	8.63
CC	1.91	3.41	2.13	4.61
DA	2.20	3.37	1.40	3.19
DB	1.17	2.45	0.80	1.71
DC	0.75	1.15	0.53	1.06
EA	1.30	1.30	—	1.13
EB	0.26	0.66	0.29	0.48
EC	0.21	0.38	0.10	0.26

Table 5. Enrichment coefficient

	α	
Alloy	Equation (6)	Equation (9)
BC	1.19	1.10
CC	1.25	1.20
DC	1.56	1.75

Calculated values are compared in Table 5 with measured enrichment levels. Discrepancies could be caused by insufficient accurancy in the measurement. As the small precipitate size, less than 1 μm in the lower chromium content alloys, increases the uncertainty of the volume fraction measurement significantly, evaluation of α from diffusional analysis (Equation (9)) was adopted. The resulting values are seen in Table 6 not to vary significantly with temperature or gas composition. Thus alloy composition is the main factor influencing chromium enrichment.

5.2 Parabolic rate constant as a function of $N_{Cr}^{(0)}$

Measured values of $k_p^{(i)}$ and calculated enrichment factores were used to construct the plots displayed in Fig. 4 for Equation (7). Agreement is generally good. However, alloys with high iron levels deviated from linearity at the higher chromium content above the expected values, and the best linear fitting did not always pass through the origin. This agrees with previous observations of internal oxidation of Ni-Cr alloys in Ni/NiO Rhines packs [10,11]. This might be an indication of coarser precipitate interfaces providing pathways for short circuit diffusion. The best agreement with *Wagner's* model was found for the high nickel bearing alloys.

Table 6. Enrichment factor calculated from Equation (9)

	Rhines pack		CO-CO_2	
Alloy	1100 °C	1150 °C	1100 °C	1150 °C
AA	1.03	1.04	1.03	1.03
AB	1.05	1.06	1.05	1.05
AC	1.06	1.08	1.07	1.07
BA	1.04	1.05	1.04	1.04
BB	1.06	1.07	1.05	1.06
BC	1.13	1.12	1.07	1.07
CA	1.10	1.11	1.09	1.09
CB	1.12	1.21	1.14	1.13
CC	1.17	1.23	1.16	1.18
DA	1.20	1.29	1.28	1.30
DB	1.38	1.43	1.49	1.55
DC	1.52	1.73	1.66	1.77
EA	1.29	1.57	—	1.62
EB	1.91	1.92	1.86	2.12
EC	2.03	2.27	2.60	2.59

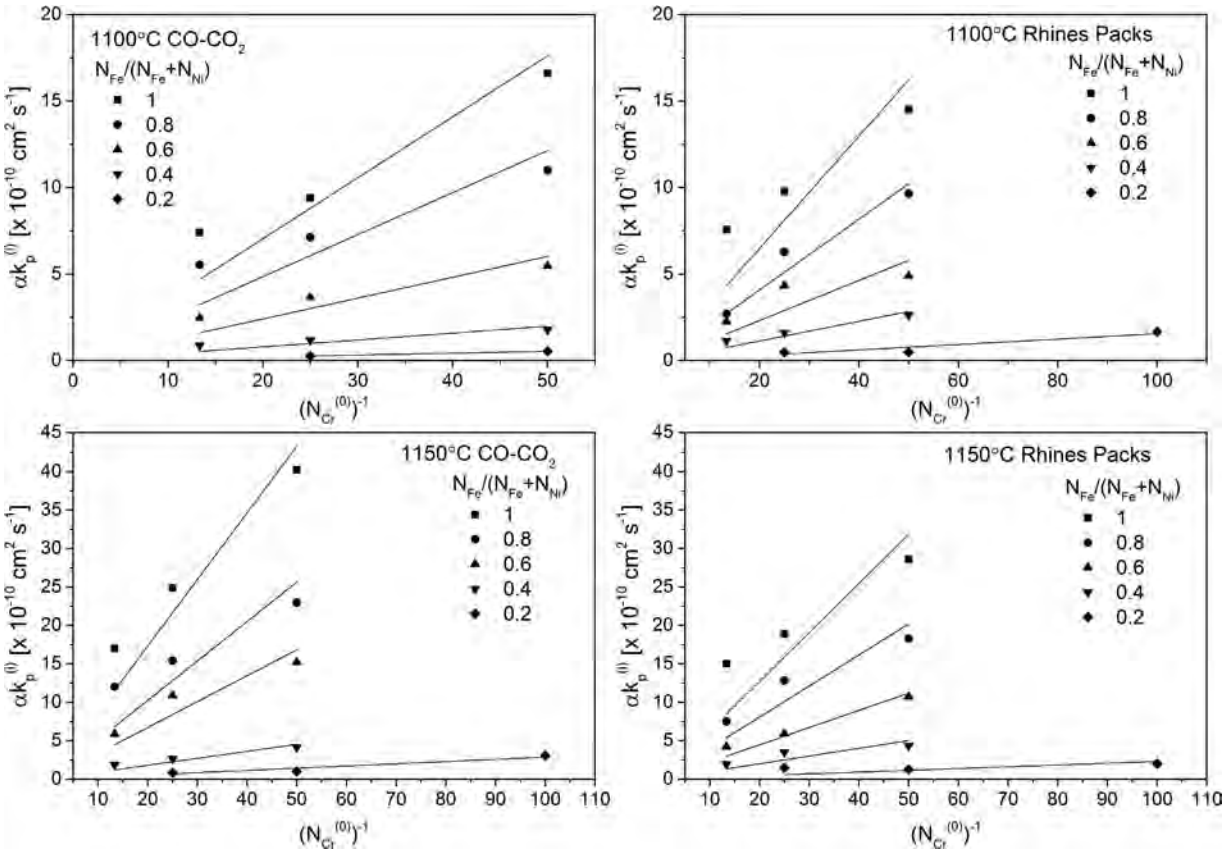

Figure 4. Plots of $\alpha k_p^{(i)}$ as function of $(N_{Cr}^{(o)})^{-1}$

5.3 Effective stoichiometric coefficient

The internal oxidation zone was characterized using EDS, which revealed that for all alloys, the internal oxides were composed of iron-rich spinel near the surface and chromium oxide near the oxidation front. The formation of the two oxides is explained by their relative thermodynamic stability, with lower oxygen activity being needed to form the chromium oxide compared to iron spinel. Oxygen diffuses inwards, reacting first with chromium to form chromium oxide. However, this chromium oxide can react with oxygen and iron to form spinel where oxygen and metal activities are sufficient high to make spinel stable

$$Fe + \frac{1}{2}O_2 + Cr_2O_3 = FeCr_2O_4 \qquad (11)$$

The stoichiometric coefficients for chromium oxide and spinel are 1.5 and 2, respectively. In order to apply *Wagner's* model, an effective stoichiometric coefficient was calculated using

$$\nu_{eff} = 2\frac{X_T}{X_i} + 1.5\left(1 - \frac{X_T}{X_i}\right) \qquad (12)$$

where X_T is the depth of the transition of spinel to chromium oxide and X_i is the depth of the internal oxidation front. Chromium oxide displays a higher contrast than spinel in backscattered electron SEM, thus enabling easy measurement of X_T in high contrast micrographs, as shown in Fig. 5. The small error arising from the non-instantaneous conversion of Cr_2O_3 to spinel, and the consequent imprecision in X_T (Fig. 5), is ignored.

The resulting values of the effective stoichiometric coefficient for the highest chromium content alloys are plotted in Fig. 6. It is seen that values decrease with nickel additions and do not vary significantly with temperature or gas composition, and thus the average value is chosen. An alternative formula given by *Ueda* et al. [17] based on *Meijering's* analysis [18] yields values which differ by 5% on average from those obtained with Equation (12).

5.4 Permeability calculation

Oxygen permeability values were deduced by linear regression using Equation (7). The slopes obtained from the plots in Fig. 4 were multiplied by the measured stoichiometric coefficient to yield oxygen permeability. The results are shown in Fig. 7, where for the sake of completeness, data for pure nickel [9,10] are included.

5.4.1 Effect of temperature

In both gas environments, permeability increases with temperature for all alloy compositions. Permeability also increases with iron content in a non-ideal way at each temperature. Clearly, the

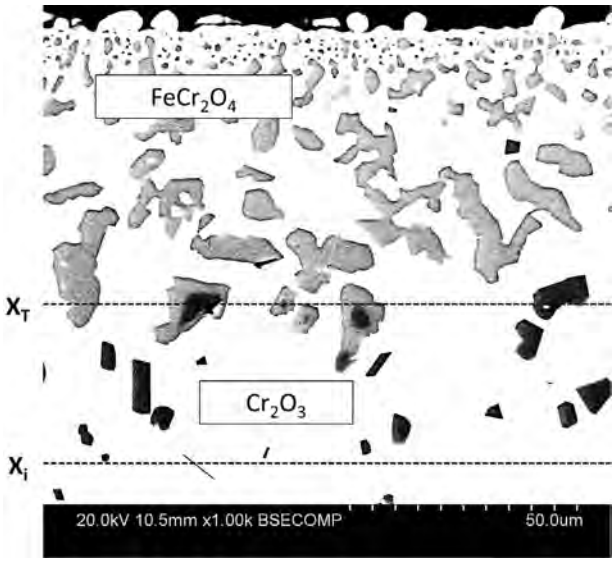

Figure 5. BSE-SEM cross-section of alloy DC reacted for 100 h at 1150 °C in CO-CO_2

use of a law of mixtures to approximate alloy oxygen permeability from pure metal values is not appropriate.

The effect of temperature is much more significant in the higher iron alloys, particularly in CO-CO_2 gas mixtures, where permeability increases by a factor of up to two from 1100 °C to 1150 °C. The same alloys in Rhines packs show a similar increase with temperature, although absolute permeability values are lower.

5.4.2 Effect of gas composition

Results at both temperatures reflect a similar qualitative effect of gas composition, with larger permeability values obtained with CO-CO_2 for the iron-rich alloys, and a transition to equal or slightly lower values in CO-CO_2 gases for high nickel alloys.

The largest difference with gas composition is found for iron rich alloys at 1150 °C, where $N_O^{(s)} D_O$ is significantly higher in

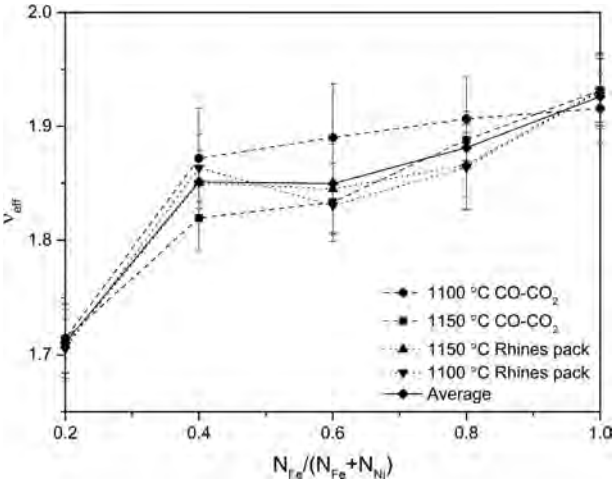

Figure 6. Effective stoichiometric coefficient for Fe-Ni alloys with highest chromium content

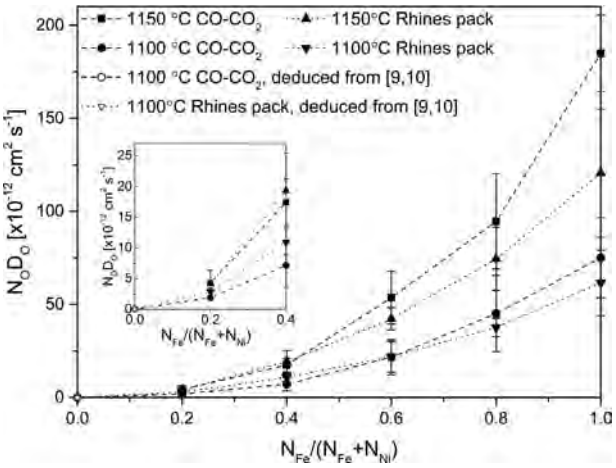

Figure 7. Oxygen permeability as a function of alloy composition. Pure Ni data deduced from [9,10]

carbon containing environments than that in carbon free gas. The difference is much smaller at 1100 °C. In fact, all alloy compositions at the lower temperature showed undistinguishable oxygen permeability values in the two reaction gases, which are within experimental uncertainties.

It is noteworthy that the maximum carbon solubility in the Fe-Ni system is found for pure iron [19], which coincides with the location of the maximum difference in oxygen permeability found between carbon-bearing and carbon-free reaction gases. Also, the minimum of carbon solubility is located near $N_{Fe}/(N_{Fe}+N_{Ni}) = 0.3$, which agrees with results where measured permeabilities are the same for both conditions at 1150 °C, and where carbon exerts the smallest effect. However, this is not verified at 1100 °C, where similar values between both environments are located at $N_{Fe}/(N_{Fe}+N_{Ni}) = 0.6$. This indicates that the interaction between carbon and oxygen solutes also depends on temperature and is not simply described.

6 Conclusions

High temperature oxygen permeability in the Fe-Ni system was determined using internal oxidation measurements in Fe-Cr and Fe-Ni-Cr alloys at the Fe-FeO equilibrium oxygen potential, in Rhines packs and CO-CO_2 gases. Internal oxidation followed parabolic kinetics in all cases, with the formation of discrete internal precipitates. Increases in chromium and nickel contents increased the size of internal precipitates. No preferential penetration was observed along grain boundaries, reflecting predominantly bulk diffusion of oxygen. With respect to gas composition, higher oxygen permeability was found for iron-rich alloys under CO-CO_2 mixtures than in carbon-free gas, this effect being more significant at 1150 °C. This finding suggests that carbon-rich atmospheres might increase the chromium level required to form a protective chromia scale on iron-based austenitic alloys at high temperatures. Data at additional temperatures are needed in order to determine activation energies.

Acknowledgements: Financial support from the Australian Research Council under its Discovery Scheme is gratefully acknowledged.

7 References

[1] C. Wagner, *Z. Elektrochem.* **1959**, *63*, 772.
[2] R.A. Rapp, *Acta Metall.* **1961**, *9*, 730.
[3] J.-B. Leblond, *Oxid. Met.* **2011**, *75*, 93.
[4] W. Zhao, Y. Kang, J. Orozco, B. Gleeson, *Oxid. Met.* **2015**, *83*, 187.
[5] C.S. Giggins, F.S. Pettit, *Oxid. Met.* **1980**, *14*, 363.
[6] J.P. Abellán, T. Olszewski, H.J. Penkalla, G.H. Meier, L. Singheiser, W.J. Quadakkers, *Mater. High. Temp.* **2009**, *26*, 63.
[7] G. Meier, K. Jung, N. Mu, N. Yanar, F. Pettit, J. Pirón Abellán, T. Olszewski, L. Nieto Hierro, W. Quadakkers, G. Holcomb, *Oxid. Met.* **2010**, *74*, 319.
[8] J.H. Swisher, E.T. Turkdogan, *Trans. AIME* **1967**, *239*, 426.
[9] J.-W. Park, C. Altstetter, *Metall. Trans. A* **1987**, *18*, 43.
[10] P. Guo, J. Zhang, D. Young, C. Konrad, *Oxid. Met.* **2015**, *83*, 223.
[11] F.H. Stott, G.C. Wood, D.P. Whittle, B.D. Bastow, Y. Shida, A. Martinez-Villafane, *Solid State Ionics* **1984**, *12*, 365.
[12] D.P. Whittle, Y. Shida, G.C. Wood, F.H. Stott, B.D. Bastow, *Philos. Mag. A* **1982**, *46*, 931.
[13] F. Rhines, W. Johnson, W. Anderson, *Trans. AIME* **1942**, *147*, 205.
[14] D.J. Young, *High Temperature Oxidation and Corrosion of Metals*, Elsevier Science, Amsterdam **2008**.
[15] J. Takada, S. Yamamoto, S. Kikuchi, M. Adachi, *Metall. Trans. A* **1986**, *17*, 221.
[16] G.C. Wood, F.H. Stott, D.P. Whittle, Y. Shida, B.D. Bastow, *Corros. Sci.* **1983**, *23*, 9.
[17] M. Ueda, Y. Inoue, H. Ochiai, M. Takeyama, T. Maruyama, *Oxid. Met.* **2013**, *79*, 485.
[18] J.L. Meijering, *Advances in Materials Research*, 5th ed, Wiley-Interscience, New York, **1971**.
[19] T. Wada, H. Wada, J. Elliott, J. Chipman, *Metall. Mater. Trans. B* **1971**, *2*, 2199.